A multiscale numerical modeling investigation on the significance of flow partitioning for the development of quartz c-axis fabrics

Ankit Bhandari[1], Dazhi Jiang[1,2]

[1]*Department of Earth Sciences, Western University, 1151 Richmond Street, London, Ontario N6A 5B7, Canada*

[2]*Department of Geology, Northwest University, Xi'an China*

Abstract: Quartz c-axis fabrics in natural mylonites can vary to such an extent that they apparently give opposite senses of shear in a single thin section. Many hypotheses have been invoked to explain this. Here, we couple our self-consistent multiscale approach for flow partitioning with the visco-plastic self-consistent model for crystallographic fabric simulation to investigate quartz c-axis fabric development. Quartz aggregates are regarded as microscale Eshelby inhomogeneities embedded in a macroscale medium whose effective rheology is represented by a hypothetical homogeneous equivalent medium which is rheologically isotropic or has a planar anisotropy. We reproduced the observed quartz c-axis fabrics. We found that, although the microscale flow fields are distinct from one another and from the macroscale flow, the microscale vorticity in every inhomogeneity has the same sense as the macroscale vorticity. This implies that one can use the average of the microscale vorticity axes determined through the crystallographic vorticity axis analysis to obtain the macroscale vorticity axis. However, quartz c-axis fabrics cannot be used to determine the vorticity number where flow partitioning is significant.

Keywords: quartz c-axis fabric; flow partitioning; multiscale modeling, MOPLA; VPSC

[1] Corresponding author: email djiang3@uwo.ca

1. Introduction:

Quartz c-axis fabrics are widely used to infer flow kinematics (e.g. Lister and Hobbs, 1980; Price, 1985; Simpson and Schmid, 1983) as well as deformation temperature (e.g. Faleiros et al., 2016; Law, 2014) and mechanisms (e.g. Schmid and Casey, 1986; Stipp et al., 2002) of ductile shear zones in Earth's lithosphere. In terms of kinematics, the asymmetry of a c-axis fabric with respect to the shear zone coordinates is routinely used to infer sense of shear (e.g. Lister, 1977; Lister and Price, 1978; Lister and Williams, 1979; Menegon et al., 2008; Price, 1985). Fig.1 summarizes the standard models for this practice (e.g. Passchier and Trouw, 2005). Note we have adopted the convention of Lister (1977) to present the c-axis fabrics whereby the shear plane (C-foliation) is vertical east west and the shear direction (the Lc-lineation of Lin et al., 2007) is horizontal east. This convention differs from the one that orients the S-foliation east west and Ls-lineation horizontal east (e.g., Passchier and Trouw 2005). Natural quartz c-axis fabrics mainly comprise of single- and cross-girdles. In the coordinate system used here (Fig.1), the cross-girdle has its dominant girdle normal to the shear plane and the weaker girdle inclined antithetically to the shear sense (Fig.1a). Single c-axis girdles either incline antithetically to the shear sense or are nearly normal to the shear plane (Fig.1b, c). Point maxima within the girdles may lie at the periphery, the center, or intermediate positions between the periphery and the center. These are interpreted as reflecting the slip systems during deformation (e.g. Mainprice et al., 1986; Okudaira et al., 1995; Schmid and Casey, 1986; Simpson and Schmid, 1983). The models summarized in Fig.1 were based on numerical modeling of pure quartz aggregates using the Taylor-Bishop Hill model (e.g. Lister, 1977; Lister and Hobbs, 1980; Lister and Williams, 1979) and the visco-plastic self-consistent (VPSC) model (e.g. Morales et al., 2011; Nie and Shan, 2014; Wenk et al., 1989). Both model methods predicted that the c-axis girdle is antithetic or normal to the shear zone boundary in the coordinate system used here. Modeling has never generated girdles synthetically-inclined to the shear plane.

However, synthetically-inclined girdles have been observed in both natural shear zones (e.g. Keller and Stipp, 2011; Kilian et al 2011, Law et al., 2010; Little et al., 2016) and creep experiments of quartz aggregates (e.g. Heilbronner and Tullis, 2006; Kilian and Heilbronner, 2017). Heilbronner and Tullis (2006) suggested that the synthetical orientation is due to rotation with vorticity of earlier antithetic girdles as finite strain increases. But this is not supported by

any numerical modeling work with fairly large shear strains (up to 5, e.g. Jessell and Lister, 1990; Morales et al., 2011). Little et al (2016) suggested that general plane-strain flows may lead to synthetically-inclined c-axis girdles. The VPSC models of Takeshita et al. (1999) and Nie and Shan (2014) considered such flows but did not produce any synthetically-inclined c-axis girdles. However, their model did not consider cases where prism<a> and rhomb<a> slips are more significant than basal<a> slip. Through VPSC modeling, Keller and Stipp (2011) produced synthetically-inclined c-axis girdle with rhomb <a>, prism <a>, and prism <c> all active and all more significant than the basal <a> slip system. However, there are natural samples with synthetically-inclined c-axis girdles (e.g. Little et al 2016, Kilian et al 2011; Law et al 2010) that were clearly produced in the temperature range ~350-550°C much below that required for the activation of prism <c> slip (Toy et al., 2008). Furthermore, c-axis fabrics with both synthetically- and antithetically-inclined c-axis girdles have been observed in the same thin section (Kilian et al., 2011 their fig. 8, 9). Therefore, it is important to clarify if the combination of rhomb<a> and prism<a> slip, without prism <c>, can generate these synthetically-inclined c-axis girdles.

The standard models summarized in Fig.1 are based on the deformation of pure quartz aggregates under limited (mostly simple shearing) single-scale uniform flows (e.g. Lister et al., 1978; Lister and Hobbs, 1980; Lister and Williams, 1980; Keller and Stipp, 2011; Morales et al., 2014; Nie and Shan, 2014; Wenk et al., 1989). The spatial variation of quartz c-axis fabrics is a manifestation of heterogeneous deformation and, we suspect, is related to flow partitioning (e.g., Jiang, 1994a, 1994b; Lister and Williams, 1983) and strain buildup in rheologically distinct domains. Most natural mylonites are made of polyphase minerals in which the microscale rheology varies from one domain to another which facilitates flow partitioning. In fact, many authors have referred to flow partitioning qualitatively (e.g., Killian et al. 2011; Garcia Celma, 1982; Jerabek et al., 2007; Larson et al., 2014; Law, 1987; Lister and Price, 1978; Passchier, 1983; Pauli et al., 1996; Peternell et al., 2010) to explain observed c-axis fabric variations.

In this contribution, we apply a multiscale numerical modeling approach to quantitatively investigate the consequence of flow partitioning on the development of quartz c-axis fabrics and compare our modeling results with natural and experimental observations. Specifically, we use the mylonite thin-section photomicrograph of Killian et al (2011, Fig.8 there) as a model and

seek to understand if flow partitioning can produce the observed variation in quartz c-axis fabrics.

2. Approach

Fig.2a shows the thin-section photomicrograph from Kilian et al (2011). The rock is comprised of quartz domains (from which c-axis fabrics were presented), feldspar porphyroclasts, and a matrix of fine-grained quartz, feldspar, and mica. According to Kilian et al. (2011), the microstructure was produced in a simple shearing flow which is consistent with the geometric pattern of the foliation (Ramsay, 1980; Ramsay and Graham, 1970). In this investigation, we consider plane-strain general shearing flows as the bulk flow field to understand how the partitioning of the bulk flow into rheologically distinct quartz domains may affect the c-axis fabrics in those domains. Our method here also applies to any 3D general shearing flows (e.g. Jiang and Williams, 1998).

In the coordinate system used in this investigation (Fig.2c), a general plane-strain general shearing flow is defined by the following Eulerian velocity gradient tensor:

$$\mathbf{L}=\begin{pmatrix} \dot{\varepsilon} & \dot{\gamma} & 0 \\ 0 & -\dot{\varepsilon} & 0 \\ 0 & 0 & 0 \end{pmatrix} \quad (1)$$

where $\dot{\gamma}$ is the shear strain rate for the simple shearing component and $\dot{\varepsilon}$ is the strain rate parallel to the X-axis. The flow in Eq.1 corresponds to a kinematic vorticity number $W_k = \frac{\dot{\gamma}}{\sqrt{4\dot{\varepsilon}^2 + \dot{\gamma}^2}}$ (Jiang and White, 1995; Li and Jiang, 2011; Truesdell, 1953). We consider the variation of the flow by varying W_k from 0 to 1.

The progression of the finite strain is measured by a strain intensity defined as $\rho = \sqrt{\left(ln\frac{s_1}{s_2}\right)^2 + \left(ln\frac{s_2}{s_3}\right)^2}$ where s_1, s_2, s_3 are the three principal stretches ($s_1 > s_2 > s_3$) of the

finite strain ellipsoid (e.g., Yang et al., 2019). In the event of simple shearing ($W_k = 1$), the strain can also be measured by the shear strain γ . The relation between γ and ρ in simple shearing situation is shown in Fig.3.

We use the Visco-Plastic-Self-Consistent(VPSC) model, originally due to Molinari et al (1987) and further developed by Lebensohn and Tome (1993), to simulate the quartz c-axis fabric development in a flow field. Specifically, VPSC7 (Lebensohn and Tomé, 2009) for Windows is used in this investigation. We track the c-axis evolution of 500 quartz crystals whose initial orientations are randomly distributed in 3D space (Jiang 2007b). The initial shapes of grains are equant. The crystal shapes evolve with strain and the grain fragmentation scheme of Beyerlein et al. (2003) is used to limit the aspect ratio of quartz grains to mimic some effect of dynamic recrystallization. The VPSC output of c-axis data are plotted using the MTEX toolbox (Bachmann et al., 2010). Since we are concerned with variation in quartz c-axis fabrics, we present pole figures of the (0001) directions here. Pole figures of other crystal directions are provided in the supplementary material.

The relative activity of slip systems is modulated in VPSC by their relative critical resolved shear stress (CRSS). A lower CRSS corresponds to higher activity. For quartz, the CRSS for a slip system is largely temperature dependent with basal <a> slip occurring at about 350-500°C, rhomb<a> and prism<a> slip at ~ 500-600°C, and prism<c> slip at >650°C (e.g. Toy et al., 2008). Table 1 summarizes the slip system combinations used in this study based on previous work (e.g. Lister and Paterson, 1979; Morales et al., 2014; Wenk et al., 1989). They are labelled as Model-A to F. Morales et al (2014) and Keller and Stipp 2011) made a distinction between rhomb (+) slip{r} in <a> direction and rhomb (-) slip{z} in <a> direction in their modelling works. This distinction may be important in regime 1 dislocation creep (Hirth and Tullis, 1992) but it is not necessary for our work here on the effect of flow partitioning.

In the single scale case, the flow field defined in Eq.1 is used in the VPSC directly for the simulation of the resulting quartz c-axis fabric development. In the multiscale case, Eq.1 defines the bulk macroscale flow which must be partitioned into different rheologically distinct quartz domains (Figs. 2b and d) before the quartz c-axis fabric development in those domains can be simulated with VPSC. We use the self-consistent Multi Order Power Law Approach (MOPLA) (Jiang and Bentley 2012; Jiang 2016, 2014; Qu et al., 2016; and Lu 2020) to obtain the

partitioned flow fields in quartz domains. The multiscale approach can be illustrated using the thin section sample in Fig.2a as follows: Quartz domains, feldspar porphyroclasts, and mica seams are referred to as Rheologically Distinct Elements (RDEs). The sample as a whole was subjected to a *macroscale* flow field like Eq.1. In micromechanics terms, the macroscale flow is the bulk flow *averaged* on a Representative Volume Element (RVE) which represents the mineral assemblage for the sample. It is reasonable to regard the thin section as a section of the RVE for the macroscale flow. The *microscale* flow field in each constituent RDE such as a quartz domain is distinct and differs from the macroscale flow, because each RDE is unique in its rheology, shape, and orientation (Eshelby, 1957; Mura, 1987; Jiang 2014, 2016). Clearly, it is the microscale (or partitioned) flows in quartz domains that are responsible for the quartz c-axis fabric development.

In MOPLA, an RDE is regarded as an ellipsoidal Eshelby inhomogeneity embedded in and interacting with the macroscale material (Fig.2d). The rheology of the latter is approximated by a homogeneous effective medium (HEM) and obtained from the rheologies of the constituent RDEs from a set of homogenization equations. The microscale or partitioned flows in an RDE is related to the macroscale flow, which is assigned by Eq.1, by a set of partitioning equations (for details, see Jiang 2014, 2016). The partitioning and homogenization equations are solved simultaneously to obtain the partitioned flow fields and the macroscale rheology. As the relevant rheology for mylonites are power-law viscous (Kohlstedt et al., 1995), the MOPLA formulation adopts a linearization approach (Lebensohn and Tomé, 1993; Molinari et al., 1987) where linearized viscosities such as tangent viscosities are used in the formulation. As we are concerned with quartz c-axis fabric development, we specifically use MOPLA to calculate the partitioned flow fields within quartz domains.

We consider two situations for the rheology of the quartz RDEs and HEM. In the first, both the RDEs and the HEM are isotropic. The rheological contrast between an RDE and the HEM is reduced to an effective viscosity ratio r between the RDE to the HEM. We do not consider the rheological anisotropy development in HEM as a result of fabric buildup with strain because anisotropic rheological response of the constituent RDEs are not available. Because of power-law rheology, r varies with time. We thus consider a range of constant r values. The quartz aggregates in Fig.2a all have convex shapes with surrounding matrix material wrapping

around them, suggesting that quartz RDEs were rheologically stronger ($r > 1$) than the ambient HEM. But r cannot be too high (e.g., $r > 10$) because of power-law rheology or the quartz RDEs would behave like rigid clasts (Jiang, 2007a; Xiang and Jiang, 2013) with no c-axis fabric formation. We consider the situations of r being 2, 5, and 10. The situation of $r = 0.5$ is also considered here for comparison to show what the c-axis fabrics might be like if quartz RDEs were mechanically weaker than the ambient medium.

In the second situation, we consider isotropic RDEs in a HEM of simple planar anisotropy which approximates a foliated and/or layered material like natural mylonites. The rheology of such a HEM can be characterized by two distinct viscosities: η_n , the normal viscosity for the resistance to pure shearing along and perpendicular to the layering, and η_S the shear viscosity measuring the resistance to shearing parallel to the layering (e.g. Jiang, 2016; Fletcher, 2009; Johnson and Fletcher, 1994) . The strength of anisotropy is measured by the ratio m of η_n to η_S . For foliated and layered rocks, $m > 1$ (Treagus, 2003).The rheological contrasts between the isotropic quartz RDE and HEM can be defined by the following two parameters: the ratio, r_{eff} , between the viscosity of the RDE to η_n and m. In such case, the effective viscosity of the RDE is simply given by $r_{eff}\eta_n$. Similar to the isotropic cases, we consider r_{eff} being 0.5, 2, 5, and 10. Fig. 4 shows the geometric relation between the flow field and the plane of anisotropy. Macroscale flow is simple shear with shear plane parallel to X-Z plane.

To cover the shape variation of quartz RDEs, we considered three reference initial shapes: prolate (5:1:1), oblate (5:5:1), sphere (1:1:1) and initial triaxial RDEs with long and short semi-axial length fixed to 5 and 1 respectively and intermediate semi-axial length ranging from 2-4. These initial RDEs will deform into various possible triaxial shapes in nature. The initial orientations of the RDEs are defined by spherical angles (Jiang, 2007b, 2007a) which are randomly assigned.

The partitioned flow for a quartz RDE computed from MOPLA is used as the input flow field to simulate the quartz c-axis fabrics in that RDE through the VPSC model. Because the partitioned flow field in any given RDE is non-steady as the RDE continuously changes shape and orientation during deformation, the coupled computation between MOPLA and VPSC is carried out as follows: With a given macroscale flow field defined in Eq.1, we use MOPLA

algorithm implemented in MATLAB (Lu, 2020; Jiang, 2016, 2014, 2007a; Jiang and Bentley, 2012; Qu et al., 2016) to calculate the partitioned flow in every quartz RDE, which is expressed as a velocity gradient tensor. We export to a data file the RDE velocity gradient tensor for every prescribed macroscale strain increment until a pre-set macroscale finite strain is reached. This data file is then used as input flows into the VPSC code to calculate the c-axis fabric evolution within the RDEs as macroscale strain increases until the set magnitude. The velocity gradient tensor files for all the RDEs are available in the supplementary material.

3. Results:

As mentioned above, we have simulated quartz c-axis fabric development in three situations. The first is in homogeneous macroscale plane-strain general shearing flows, without flow partitioning, with quartz slip system combinations that have not been covered by previous studies. The second situation is when rheologically distinct quartz domains are within an isotropic HEM, and the third is when the quartz domains are within a HEM of planar anisotropy.

3.1 Quartz c-axis fabric development in homogeneous plane-strain general shearing flows

Figs.5 and 6 present quartz c-axis fabrics produced for models-A-F (rows) under uniform macroscale flows of plane-strain general shearing from $W_k = 0$ to $W_k = 1$ (columns), at macroscale strain states $\rho = 2$ and 6.

In pure shearing ($W_k = 0$), for models-A, C, and D, peripheral c-axis maxima form and remain at the maximum shortening direction regardless of strains (Figs. 5a,d, m,p,6a,d). For model-B, a cross-girdle (Figs 5g) form at $\rho = 2$, with its central segment lying along the maximum shortening direction. A single girdle is produced lying along the maximum shortening direction (Figs. 5j) at $\rho = 6$. For models-E and F, peripheral maxima develop and remains at the maximum stretching direction at both strain states (Figs. 6g, j, m, p).

When $0 < W_k \leq 1$, for models-A, C, and D and at $\rho = 2$, peripheral c-axis maxima are developed inclining antithetically to the shear sense (Figs. 5b, c, n, o, 6b, c). As W_k increases , the angle between the peripheral c-axis maxima and the shear plane normal increases. The peripheral

maxima rotate with macroscale vorticity as finite strain increases but do not pass the shear plane normal (Figs. 5f, l, q, r, 6f). For model-B, a cross-girdle, with its central segment lying normal to the shear plane, is formed at $\rho = 2$ (Figs 5 h, i). At $\rho = 6$, this cross-girdle becomes a single girdle lying normal to the shear plane (Figs. 5 k, l). In some general shear ($0 < W_k < 1$) cases, the c-axis girdles can be slightly synthetically-inclined at $\rho = 6$ (Figs. 5e,k,6e), but the angle between the peripheral c-axis maxima and the shear plane normal is small (< 10°). For models-E and F, the c-axis peripheral maxima are synthetically-inclined near the shear direction at $\rho = 2$. The angle between the peripheral c-axis maxima and the shear direction increases with W_k (Figs.6h, i, n, o). The c-axis peripheral maxima rotate with vorticity toward the shear direction as the finite strain increases (Figs.6 k, l, q, r).

3.2 *Quartz c-axis fabric development in quartz domains embedded in an isotropic HEM*

Since models-A, B, C and D all produce similar c-axis fabrics with c-axis girdles antithetically-inclined or nearly normal to the shear plane, we only present results for model-A for multiscale deformation. Figs. 7 and 8 report ten results of c-axis fabrics produced in quartz RDEs of varying initial shapes, orientations, and viscosity ratio r under a range of macroscale flow fields. These results can be summarized as follows: When $0 < W_k \leq 1$, c-axis girdles are always antithetically-inclined (Figs.7a,b,d,e,g,h, j, k, m, n, 8a,g,j,m) regardless of initial conditions of RDEs up to the finite strain ρ ~4. With increase in finite strain, the girdles rotate with bulk vorticity (rows of Figs.7 and 8) but do not pass the shear plane normal unless $r >= 5$ (Figs. 7-i, l, o, 8-b, c, i, l, o). If the RDEs were weaker than the HEM (r = 0.5), c-axis girdles remain close to normal (Figs. 7-c) to the shear plane even at very high finite strains (ρ ~6-7). In pure shearing, a cross girdle is produced at ρ ~2 which becomes a single girdle at ρ ~6 with peripheral c-axis maxima always parallel to the maximum shortening direction (Figs.8-d, e, f).

3.3 *Quartz c-axis fabric development in quartz domains embedded in a planar anisotropic HEM*

Figs. 9a-o report c-axis fabrics developed in quartz RDEs of varying initial shapes, orientations, and viscosity ratio r_{eff}, embedded in a planar anisotropic HEM of anisotropic strength m as described in Section-2. These results can be summarized as follows: The c-axis girdles are always antithetically-inclined (Figs.9a,d,g,j,m) at ρ ~2 regardless of W_k, r_{eff}, m, initial orientations and shapes of RDEs. The girdles rotate with bulk vorticity as ρ increases (rows of

Figs.9) but do not pass the shear plane normal unless r_{eff} >= 2 (Figs. 9i, l, o). If RDEs were weaker (r_{eff} = .5), c-axis girdles are close to normal (Figs. 9c, f) to the shear plane even at high finite strains (ρ ~6-7).

4. Discussion:

In Section 2, we argued that r must be greater than 1 from microstructures (Fig.2a) but not so high that the quartz RDEs do not develop enough internal strain for c-axis fabric formation. In our modeling, we considered the range r between 2 and 10. Our modeling results show that, with basal<a>, rhomb<a>, and prism<a> slips, c-axis girdles in a quartz RDE always develop at an antithetical orientation initially. But the girdles rotate with vorticity as the macroscale finite strain increases. If the RDE is sufficiently strong ($r \geq 5$ in isotropic HEM case and $r_{eff} \geq 2$ in planar anisotropic HEM case), the girdles will rotate pass the shear zone normal and lie in the synthetical sector at high strains (ρ ~6, Figs. 7-i, l, o, 8-b, c, i, l, o, 9-i, l, o). Our modeling results show that for synthetically-inclined girdles, r should be between 5 and 10. These results are consistent with the strain gradient of the thin section (Fig.10, based on Killian et al., 2011, Fig.9 there). The antithetically-inclined c-axis peripheral maxima (yellow in Fig.10) correspond to a lower strain and synthetically-inclined c-axis peripheral maxima (red in Fig. 10) to a higher strain.

Despite the variability of the partitioned flow field in quartz RDEs, we found out that the microscale vorticity in every quartz RDE still has the same sense as the macroscale vorticity. Fig.11 shows the dot product of the unit vector $\widehat{\boldsymbol{\omega}}$ parallel to the vorticity in a RDE and the unit vector $\widehat{\Omega}$ parallel to the macroscale vorticity. $\widehat{\boldsymbol{\omega}} \cdot \widehat{\Omega}$ is positive for all quartz RDEs (a few selected ones are shown in Fig.11). In other words, there is no vorticity sense reversal in any quartz RDEs. This implies that the volume-weighted average of microscale vorticity vectors is parallel to the macroscale vorticity vector. Therefore, the crystallographic vorticity axis (CVA) analysis (Giorgis et al., 2017; Michels et al., 2015) can still be used in every quartz RDE and then the averaged microscale vorticity axes represent the macroscale vorticity axis.

Synthetically-inclined c-axis girdles have also been reported in some creep experiments on pure quartz aggregates with similar slip systems (basal<a>, rhomb<a>, and prism<a>) at high finite strains (Heilbronner and Tullis 2002, 2006). Although Keller and Stipp (2011) obtained

synthetically-inclined c-axis girdles by including prism<c> slip in their VPSC models, we have further confirmed that without prism <c> slip (our model-D), synthetically-inclined c-axis girdles cannot be produced (Figs. 5a-f), unless flow partitioning is considered. We suspect that some degree of heterogeneous strain and therefore partitioned flow was responsible for such c-axis girdle orientations. Heilbronner and Tullis (2006) themselves suggested that different domains of polycrystal aggregates might exhibit different viscosities, which could have facilitated partitioning of the flow among different domains.

Li and Jiang (2011) raised issues with the practice of vorticity estimation using rigid porphyroclasts under the assumption of steady-state homogeneous flow histories. The significance of flow partitioning as demonstrated by our modeling based on microstructures of natural mylonites raises further issues with using quartz c-axis fabrics to estimate the (macroscale) vorticity (e.g. Vissers, 1989; Wallis, 1995, 1992; Xypolias, 2009; Law, 2010). First, where quartz c-axis fabrics have resulted from partitioned flow, the steady-state flow assumption is invalid. As we have shown, there is a distinct microscale vorticity history, not a constant vorticity number, in every quartz RDE, which cannot be determined from the final c-axis fabric. In principle, the microscale vorticity in a quartz RDE does not have a simple relation to the macroscale vorticity. Second, even for the single-scale case where no flow partitioning is considered, our modeling demonstrates that the assumption commonly used in vorticity determination that the dominant c-axis girdle is perpendicular to the shear plane is not always valid.

Peripheral c-axis maxima close to the shear direction have commonly been taken to reflect prism <c> slip (Passchier and Trouw, 2005). Our modeling suggests that they can also be significantly rotated peripheral basal <a> maxima from certain quartz RDEs (Fig.8c). Larson et al (2014) have reported a possible example of this. They presented peripheral c-axis maxima close to the shear direction in a temperature condition much below that required for the activation of prism <c> and used the concept of flow partitioning to explain their observation. Our modeling lends support to this explanation.

5. Conclusions:

The co-existence of both synthetically-inclined and antithetically-inclined quartz c-axis girdles in a single thin section can be explained by flow partitioning at the thin section scale. The antithetically-inclined girdles correspond to relatively low finite strains and the synthetically-inclined girdles to high finite strains.

Although the microscale flow fields vary from one quartz RDE to another and are distinct from the macroscale flow, the sense of vorticity in every quartz RDEs remains the same as the macroscale vorticity.

Because of flow partitioning, it is not possible to estimate the vorticity number of the macroscale flow from quartz c-axis fabrics. But, it is still possible to obtain the macroscale vorticity axis by averaging the microscale vorticity axes from quartz RDEs. The latter can be obtained through the crystallographic vorticity axis analysis .

As a result of partitioned flows, the dominant quartz c-axis girdle can lie antithetical, normal, synthetical to the shear plane. The basal <a> peripheral maxima may end up lying close to the shear direction at high macroscale strains. Caution should be taken not to misinterpret these peripheral maxima as reflecting prism<c> slip.

Acknowledgements:

Numerical modeling in this paper used our own MOPLA code (Jiang 2016, 2014, 2007a, Jiang and Bentley 2012, Qu et al. 2016) coupled with the VPSC code kindly provided by R. Lebensohn (Lebensohn and Tomé 2009). Visualization used the MTEX toolbox of Bachmann et al. (2010). All model parameters are listed in Tables 1 and Section 3 of the text. We are grateful to Dr. Mengmeng Qu, Dr. Lucy X. Lu, and Rui Yang for many discussions. Mengmeng and Lucy are also thanked for their generous help with using MATLAB. DJ acknowledges financial support from Canada's Natural Science and Engineering Research Council (NSERC) through a Discovery Grant, China's National Natural Science Foundation (NSFC, grants 41472184, 41772213), and Northwest University. This paper is part of AB's ongoing PhD project at Western University.

References:

Bachmann, F., Hielscher, R., Schaeben, H., 2010. Texture analysis with MTEX- Free and open

source software toolbox. Solid State Phenom. 160, 63–68. https://doi.org/10.4028/www.scientific.net/SSP.160.63

Beyerlein, I.J., Lebensohn, R.A., Tomé, C.N., 2003. Modeling texture and microstructural evolution in the equal channel angular extrusion process. Mater. Sci. Eng. A 345, 122–138. https://doi.org/10.1016/S0921-5093(02)00457-4

Eshelby, J.D., 1957. The determination of the elastic field of an ellipsoidal inclusion, and related problems. Proc. R. Soc. London. Ser. A. Math. Phys. Sci. 241, 376 LP – 396.

Faleiros, F.M., Moraes, R., Pavan, M., Campanha, G.A.C., 2016. A new empirical calibration of the quartz c-axis fabric opening-angle deformation thermometer. Tectonophysics 671, 173–182. https://doi.org/10.1016/j.tecto.2016.01.014

Fletcher, R.C., 2009. Deformable, rigid, and inviscid elliptical inclusions in a homogeneous incompressible anisotropic viscous fluid. J. Struct. Geol. 31, 382–387. https://doi.org/10.1016/j.jsg.2009.01.006

Garcia Celma, A., 1982. Domainal and fabric heterogeneities in the Cap de Creus quartz myionites. J. Struct. Geol. 4, 443–445.

Giorgis, S., Michels, Z., Dair, L., Braudy, N., Tikoff, B., 2017. Kinematic and vorticity analyses of the western Idaho shear zone, USA. Lithosphere 9, 223–234. https://doi.org/10.1130/L518.1

Heilbronner, R., Tullis, J., 2006. Evolution of c axis pole figures and grain size during dynamic recrystallization : Results from experimentally sheared quartzite. J. Geophys. Res. Solid Earth 111, 1–19. https://doi.org/10.1029/2005JB004194

Hirth, G., Tullis, J., 1992. Dislocation creep regimes in quartz aggregates. J. Struct. Geol. 14, 145–159. https://doi.org/10.1016/0191-8141(92)90053-Y

Jerabek, P., Stunitz, H., Heilbronner, R., Lexa, O., Schulmann, K., 2007. Microstructural-deformation record of an orogen-parallel extension in the Vepor Unit , West Carpathians. J. Struct. Geol. 29, 1722–1743. https://doi.org/10.1016/j.jsg.2007.09.002

Jessell, M.W., Lister, G.S., 1990. A simulation of the temperature dependence of quartz fabrics.

Geol. Soc. Spec. Publ. 54, 353–362. https://doi.org/10.1144/GSL.SP.1990.054.01.31

Jiang, D., 2016. Viscous inclusions in anisotropic materials : Theoretical development and perspective applications. Tectonophysics 693, 116–142. https://doi.org/10.1016/j.tecto.2016.10.012

Jiang, D., 2014. Structural geology meets micromechanics: A self-consistent model for the multiscale deformation and fabric development in Earth's ductile lithosphere. J. Struct. Geol. 68, 247–272. https://doi.org/10.1016/j.jsg.2014.05.020

Jiang, D., 2007a. Numerical modeling of the motion of deformable ellipsoidal objects in slow viscous flows. J. Struct. Geol. 29, 435–452. https://doi.org/10.1016/j.jsg.2006.09.009

Jiang, D., 2007b. Numerical modeling of the motion of rigid ellipsoidal objects in slow viscous flows: A new approach. J. Struct. Geol. 29, 189–200. https://doi.org/10.1016/j.jsg.2006.09.010

Jiang, D., 1994a. Vorticity determination, distribution, partitioning and the heterogeneity and non-steadiness of natural deformations. J. Struct. Geol. 16, 121–130. https://doi.org/10.1016/0191-8141(94)90023-X

Jiang, D., 1994b. Flow variation in layered rocks subjected to bulk flow of various kinematic vorticities: theory and geological implications. J. Struct. Geol. 16, 1159–1172. https://doi.org/10.1016/0191-8141(94)90059-0

Jiang, D., Bentley, C., 2012. A micromechanical approach for simulating multiscale fabrics in large-scale high-strain zones: Theory and application. J. Geophys. Res. B Solid Earth 117. https://doi.org/10.1029/2012JB009327

Jiang, D., White, J.C., 1995. Kinematics of rock flow and the interpretation of geological structures, with particular reference to shear zones. J. Struct. Geol. 17, 1249–1265. https://doi.org/10.1016/0191-8141(95)00026-A

Jiang, D., Williams, P.F., 1998. High-strain zones : a unifed model. J. Struct. Geol. 20, 1105–1120.

Johnson, A.M., Fletcher, R.C., 1994. Folding of viscous layers : mechanical analysis and

394 interpretation of structures in deformed rock. Columbia University Press, New York.

395 Keller, L.M., Stipp, M., 2011. The single-slip hypothesis revisited : Crystal-preferred
396 orientations of sheared quartz aggregates with increasing strain in nature and numerical
397 simulation 33, 1491–1500. https://doi.org/10.1016/j.jsg.2011.07.008

398 Kilian, R., Heilbronner, R., 2017. Analysis of crystallographic preferred orientations of
399 experimentally deformed Black Hills Quartzite 1095–1117.

400 Kilian, R., Heilbronner, R., Stünitz, H., 2011. Quartz microstructures and crystallographic
401 preferred orientation : Which shear sense do they indicate ? J. Struct. Geol. 33, 1446–1466.
402 https://doi.org/10.1016/j.jsg.2011.08.005

403 Kohlstedt, D.L., Evans, B., Mackwell, S.J., 1995. Strength of the lithosphere: constraints
404 imposed by laboratory experiments. J. Geophys. Res.

405 Larson, K.P., Lamming, J.L., Faisal, S., 2014. Microscale strain partitioning ? Differential quartz
406 crystallographic fabric development in Phyllite , Hindu Kush , Northwestern Pakistan. Solid
407 Earth 5, 1319–1327. https://doi.org/10.5194/se-5-1319-2014

408 Law, R.D., 2014. Deformation thermometry based on quartz c -axis fabrics and recrystallization
409 microstructures : A review. J. Struct. Geol. 66, 129–161.
410 https://doi.org/10.1016/j.jsg.2014.05.023

411 Law, R.D., 1987. Heterogeneous deformation and quartz crystallographic fabric transitions:
412 natural examples from the moine thrust zone at the stack of glencoul, northern assynt. J.
413 Struct. Geol. 9, 819–833. https://doi.org/10.1016/0191-8141(87)90083-6

414 Law, R.D., Mainprice, D., Casey, M., Lloyd, G.E., Knipe, R.J., Cook, B., Thigpen, J.R., 2010.
415 Moine Thrust zone mylonites at the Stack of Glencoul: I – microstructures, strain and
416 influence of recrystallization on quartz crystal fabric development. Geol. Soc. London,
417 Spec. Publ. 335, 543–577. https://doi.org/10.1144/SP335.23

418 Lebensohn, R.A., Tomé, C.N., 2009. Manual for Code Visco-Plastic Self-consistent(VPSC)
419 Version 7c.

420 Lebensohn, R.A., Tomé, C.N., 1993. A self-consistent anisotropic approach for the simulation of

421 plastic deformation and texture development of polycrystals: Application to zirconium
422 alloys. Acta Metall. Mater. 41, 2611–2624. https://doi.org/10.1016/0956-7151(93)90130-K

423 Li, C., Jiang, D., 2011. A critique of vorticity analysis using rigid clasts. J. Struct. Geol. 33, 203–
424 219. https://doi.org/10.1016/j.jsg.2010.09.001

425 Lin, S., Jiang, D., Williams, P.F., 2007. Importance of differentiating ductile slickenside
426 striations from stretching lineations and variation of shear direction across a high-strain
427 zone. J. Struct. Geol. 29, 850–862. https://doi.org/10.1016/j.jsg.2006.12.006

428 Lister, G.S., 1977. Discussion: Crossed-girdle c-axis fabrics in quartzites plastically deformed by
429 plane strain and progressive simple shear. Tectonophysics 39, 51–54.
430 https://doi.org/10.1016/0040-1951(77)90087-7

431 Lister, G.S., Hobbs, B.E., 1980. The simulation of fabric development during plastic deformation
432 and its application to quartzite: the influence of deformation history. J. Struct. Geol. 2, 355–
433 370. https://doi.org/10.1016/0191-8141(80)90023-1

434 Lister, G.S., Paterson, M.S., 1979. The simulation of fabric development during plastic
435 deformation and its appfication to quartzite: fabric transitions. J. Struct. Geol. 1, 99–115.

436 Lister, G.S., Paterson, M.S., Hobbs, B.E., 1978. The simulation of fabric development in plastic
437 deformation and its application to quartzite: the model. Tectonophysics 45, 107–158.

438 Lister, G.S., Price, G.P., 1978. Fabric development in a quartz-feldspar mylonite.
439 Tectonophysics 49, 37–78.

440 Lister, G.S., Williams, P.F., 1983. The partitioning of deformation in flowing rock masses.
441 Tectonophysics 92, 1–33.

442 Lister, G.S., Williams, P.F., 1980. Fabric development in shear zones : theoretical controls and
443 observed phenomena. J. Struct. Geol. 1, 283–297.

444 Little, T.A., Prior, D.J., Toy, V.G., 2016. Are quartz LPOs predictably oriented with respect to
445 the shear zone boundary?: A test from the Alpine Fault mylonites, New Zealand.
446 Geochemistry, Geophys. Geosystems 17, 981–999. https://doi.org/10.1002/2015GC006145.

447 Mainprice, D., Bouchez, J.L., Blumenfeld, P., Tubià, J.M., 1986. Dominant c slip in naturally

448 deformed quartz: Implications for dramatic plastic softening at high temperature. Geology
449 14, 819–822. https://doi.org/10.1130/0091-7613(1986)14<819:DCSIND>2.0.CO;2

450 Menegon, L., Pennacchioni, G., Heilbronner, R., Pittarello, L., 2008. Evolution of quartz
451 microstructure and c -axis crystallographic preferred orientation within ductilely deformed
452 granitoids (Arolla unit , Western Alps). J. Struct. Geol. 30, 1332–1347.
453 https://doi.org/10.1016/j.jsg.2008.07.007

454 Michels, Z.D., Tikoff, B., Kruckenberg, S.C., Davis, J.R., 2015. Determining vorticity axes from
455 grain-scale dispersion of crystallographic orientations. Geology 43, 803–806.
456 https://doi.org/10.1130/G36868.1

457 Molinari, A., Canova, G.R., Ahzi, S., 1987. A self consistent approach of the large deformation
458 polycrystal viscoplasticity. Acta Metall. 35, 2983–2994. https://doi.org/10.1016/0001-
459 6160(87)90297-5

460 Morales, L.F.G., Lloyd, G.E., Mainprice, D., 2014. Tectonophysics Fabric transitions in quartz
461 via viscoplastic self-consistent modeling part I : Axial compression and simple shear under
462 constant strain. Tectonophysics 636, 52–69. https://doi.org/10.1016/j.tecto.2014.08.011

463 Morales, L.F.G., Mainprice, D., Lloyd, G.E., Law, R.D., Euge, P., 2011. Crystal fabric
464 development and slip systems in a quartz mylonite : an approach via transmission electron
465 microscopy and viscoplastic self-consistent modelling. Geol. Soc. Spec. Publ. 360, 151–
466 174.

467 Mura, T., 1987. Micromechanics of defects in solids. Springer Netherlands, Dordrecht.
468 https://doi.org/10.1007/978-94-009-3489-4_3

469 Nie, G., Shan, Y., 2014. Development of quartz c-axis crossed / single girdles under simple-pure
470 shear deformation : Results of visco-plastic self-consistent modeling. J. Struct. Geol. 66,
471 261–270. https://doi.org/10.1016/j.jsg.2014.05.022

472 Okudaira, T., Takeshita, T., Hara, I., Ando, J., 1995. A new estimate of the conditions for
473 transition from basal <a> to prism [c] slip in naturally deformed quartz. Tectonophysics
474 250, 31–46.

475 Passchier, C.W., 1983. The reliability of asymmetric c-axis fabrics of quartz to determine sense

476 of vorticity. Tectonophysics 99, T9–T18. https://doi.org/10.1016/0040-1951(83)90166-X

477 Passchier, C.W., Trouw, R.A.., 2005. Foliations, Lineations and Lattice Preferred Orientation, in:
478 Microtectonics. Springer Berlin Heidelberg, Berlin, Heidelberg, pp. 67–109.
479 https://doi.org/10.1007/3-540-29359-0_4

480 Pauli, C., Schmid, S.M., Heilbronner, R.P., 1996. Fabric domains in quartz mylonites: Localized
481 three dimensional analysis of microstructure and texture. J. Struct. Geol. 18, 1183–1203.
482 https://doi.org/10.1016/S0191-8141(96)00017-X

483 Peternell, M., Hasalová, P., Wilson, C.J.L., Piazolo, S., Schulmann, K., 2010. Evaluating quartz
484 crystallographic preferred orientations and the role of deformation partitioning using EBSD
485 and fabric analyser techniques. J. Struct. Geol. 32, 803–817.
486 https://doi.org/10.1016/j.jsg.2010.05.007

487 Price, G.P., 1985. Preferred Orientations in Quartzites, in: Preferred Orientation in Deformed
488 Metal and Rocks. Elsevier, pp. 385–406. https://doi.org/10.1016/b978-0-12-744020-
489 0.50023-7

490 Qu, M., Jiang, D., Lu, L.X., 2016. An optimal scheme for numerical evaluation of Eshelby
491 tensors and its implementation in a MATLAB package for simulating the motion of viscous
492 ellipsoids in slow flows. Comput. Geosci. 96, 98–108.
493 https://doi.org/10.1016/j.cageo.2016.08.005

494 Ramsay, J.G., 1980. Shear zone geometry: A review. J. Struct. Geol. 2, 83–99.
495 https://doi.org/10.1016/0191-8141(80)90038-3

496 Ramsay, J.G., Graham, R.H., 1970. Strain variation in shear belts. Can. J. Earth Sci. 786.

497 Schmid, S.M., Casey, M., 1986. Complete fabric analysis of some commonly observed quartz C-
498 Axis patterns, in: Geophysical Monograph. https://doi.org/10.1029/GM036p0263

499 Simpson, C., Schmid, S.M., 1983. An evaluation of criteria to deduce the sense of movement in
500 sheared rocks. Geol. Soc. Am. Bull. 94, 1281–1288. https://doi.org/10.1130/0016-
501 7606(1983)94<1281:AEOCTD>2.0.CO;2

502 Stipp, M., Stünitz, H., Heilbronner, R., Schmid, S.M., 2002. The eastern Tonale fault zone: A

503 "natural laboratory" for crystal plastic deformation of quartz over a temperature range from
504 250 to 700 °C. J. Struct. Geol. 24, 1861–1884. https://doi.org/10.1016/S0191-
505 8141(02)00035-4

506 Takeshita, T., Wenk, H.R., Lebensohn, R., 1999. Development of preferred orientation and
507 microstructure in sheared quartzite: Comparison of natural data and simulated results.
508 Tectonophysics 312, 133–155. https://doi.org/10.1016/s0040-1951(99)00173-0

509 Toy, V.G., Prior, D.J., Norris, R.J., 2008. Quartz fabrics in the Alpine Fault mylonites : Influence
510 of pre-existing preferred orientations on fabric development during progressive uplift 30,
511 602–621. https://doi.org/10.1016/j.jsg.2008.01.001

512 Treagus, S.H., 2003. Viscous anisotropy of two-phase composites, and applications to rocks and
513 structures. Tectonophysics 372, 121–133. https://doi.org/10.1016/S0040-1951(03)00239-7

514 Truesdell, C., 1953. Two Measures of Vorticity. J. Ration. Mech. Anal. 2, 173–217.

515 Vissers, R.L.M., 1989. Asymmetric quartz c-axis fabrics and flow vorticity: a study using rotated
516 garnets. J. Struct. Geol. 11, 231–244. https://doi.org/10.1016/0191-8141(89)90064-3

517 Wallis, S., 1995. Vorticity analysis and recognition of ductile extension in the Sanbagawa belt,
518 SW Japan. J. Struct. Geol. 17, 1077–1093. https://doi.org/10.1016/0191-8141(95)00005-X

519 Wallis, S.R., 1992. Vorticity analysis in a metachert from the Sanbagawa Belt, SW Japan. J.
520 Struct. Geol. 14, 271–280. https://doi.org/10.1016/0191-8141(92)90085-B

521 Wenk, H.R., Canova, G., Molinari, A., Kocks, U.F., 1989. Viscoplastic Modeling of Texture
522 Development in Quartzite. J. Geophys. Res. 94, 895–906.

523 Xiang, B., Jiang, D., 2013. Small-scale ductile shear zones as transposed rheologically weak
524 domains : A numerical modeling investigation and practical application. J. Struct. Geol. 54,
525 184–198. https://doi.org/10.1016/j.jsg.2013.06.003

526 Xypolias, P., 2009. Some new aspects of kinematic vorticity analysis in naturally deformed
527 quartzites. J. Struct. Geol. 31, 3–10. https://doi.org/10.1016/j.jsg.2008.09.009

528 Yang, R., Jiang, D., Lu, L.X., 2019. Constrictional Strain and Linear Fabrics as a Result of
529 Deformation Partitioning: A Multiscale Modeling Investigation and Tectonic Significance.

Tectonics 38, 2829–2849. https://doi.org/10.1029/2019TC005490

Figure Captions:

Figure 1: Current models for interpreting quartz c-axis fabrics at low to medium temperatures ~350-550°C presented in the shear zone coordinate system. The sense of shear is dextral. Cross-girdle and single girdle c-axis fabrics are commonly observed. (a) c-axis cross girdle pattern with one girdle normal to the shear plane while the other antithetic to the shear sense. (b) a single c-axis girdle with Y-maxima, inclined either antithetically to the shear sense or normal to the shear plane. (c) a single c-axis girdle inclined either antithetically to the shear sense or normal to the shear plane. The c-axes near the periphery, the center, and in between are interpreted to reflect basal<a>, prism<a>, and rhomb<a> slips respectively.

Figure 2: Illustration of the multiscale approach used in this paper. (a) The thin section photomicrograph of a natural mylonite from Kilian et al. (2011) used as a model. (b) Sketch of (a). The thin section can be viewed as a 2D section of the representative volume element (RVE) for the shear zone material, which is composed of quartz domains, feldspar porphyroclasts, and mica seams in a fine-grained matrix. The quartz domains and feldspar clasts are referred to as Rheologically Distinct Elements (RDEs). We are concerned with partitioned flows in quartz RDEs in this paper. (c) Coordinate system to define the macroscale flow field used in modeling investigation (d) Each quartz RDE is regarded as a heterogeneous Eshelby inclusion embedded in the composite shear zone material that is idealized as the Homogeneous Equivalent Matrix (HEM). Microscale fields (strain rate $\boldsymbol{\varepsilon}$, and vorticity $\mathbf{w}$) are related to respective macroscale fields ($\mathbf{E}$ and $\mathbf{W}$) by partitioning equations, where $\mathbf{A}$ is the strain partitioning tensor, $\mathbf{S}$ and $\boldsymbol{\Pi}$ are respectively the 4^{th}-order symmetric and anti-symmetric Eshelby tensors (Jiang 2014).

Figure 3: The macroscale finite strain of the shear zone, measured by the strain intensity ρ, as a function of computation steps for varying W_k. The increase of the shear strain γ in the simple shear case ($W_k = 1$) is also plotted for comparison.

Figure 4: Geometric relation between the macroscale flow field and anisotropy plane in the planar anisotropic HEM.

Figure 5: C-axis fabrics in single-scale deformation with varying W_k from pure shearing to simple shearing and for models-A-C. The final strain intensity is between $\rho = 2$ and 6. The pole densities are contoured in multiples of uniform distribution.

Figure 6: Same as Figure 5 but for models-D-F.

Figure 7: C-axis fabrics in selected quartz RDEs in an isotropic HEM under simple shearing (W_k =1). (a)-(o) are the resultant c-axis fabrics developed. The first column presents the initial conditions for the RDEs [r : viscosity ratio of the RDE to HEM, initial shape defined by semi-axes of the RDE ($a_1 : a_2 : a_3$,where $a_1 \geq a_2 \geq a_3$), and initial orientation given by spherical angles (θ_1, Φ_1, θ_2) for general RDEs or (θ, Φ) for spheroidal RDEs] . Each row presents the results for the RDE as the macroscale strain increases.

Figure 8: Same as Figure 7 except that the macroscale flow is plane strain general shearing ($0<W_k \leq 1$).

Figure 9: C-axis fabrics in selected quartz RDEs in a HEM with planar anisotropy under simple shearing flow ($W_k = 1$) (a)-(o) are the resultant c-axis fabrics developed. The first column presents

the initial conditions for the RDEs [r_{eff} - viscosity ratio of the RDE to HEM's η_n, initial shape defined by semi-axes of the RDE ($a_1 : a_2 : a_3$,where $a_1 \geq a_2 \geq a_3$), initial orientation given by spherical angles (θ_1, Φ_1, θ_2) for general RDEs or (θ, Φ) for spheroidal RDEs, and anisotropic strength m]. Each row presents the results for the RDE as the macroscale strain increases.

Figure 10: Sketch of the thin-section sample showing c-axis fabric variation in quartz domains (based on Kilian et al., 2011, Fig. 9 there). C-axis fabrics comprise of peripheral c-axis maxima that are antithetically-inclined (yellow), nearly normal (blue), and synthetically-inclined (red) to the shear plane. The sense of shear is dextral. The arrow at the top-left shows the direction of increase in strain gradient.

Figure 11: Plot of dot product $\widehat{\boldsymbol{\omega}} \cdot \widehat{\Omega}$ with increasing macroscale strain ρ, for 50 RDEs with random initial shapes and orientations, r = 0.5, 2 and 5(rows) and W_k = 1 and .75 (columns). $\widehat{\boldsymbol{\omega}}$ and $\widehat{\Omega}$ are, respectively, the unit vectors parallel to the microscale vorticity vector in an RDE and the macroscale vorticity vector. $\widehat{\boldsymbol{\omega}} \cdot \widehat{\Omega}$ is close to unity for the RDEs. Therefore, the microscale vorticity vectors are always of the same sense as and nearly parallel to the macroscale vorticity vector.

Table 1: Quartz slip systems and the relative CRSS values for different models used in VPSC simulation.

Figure 1.

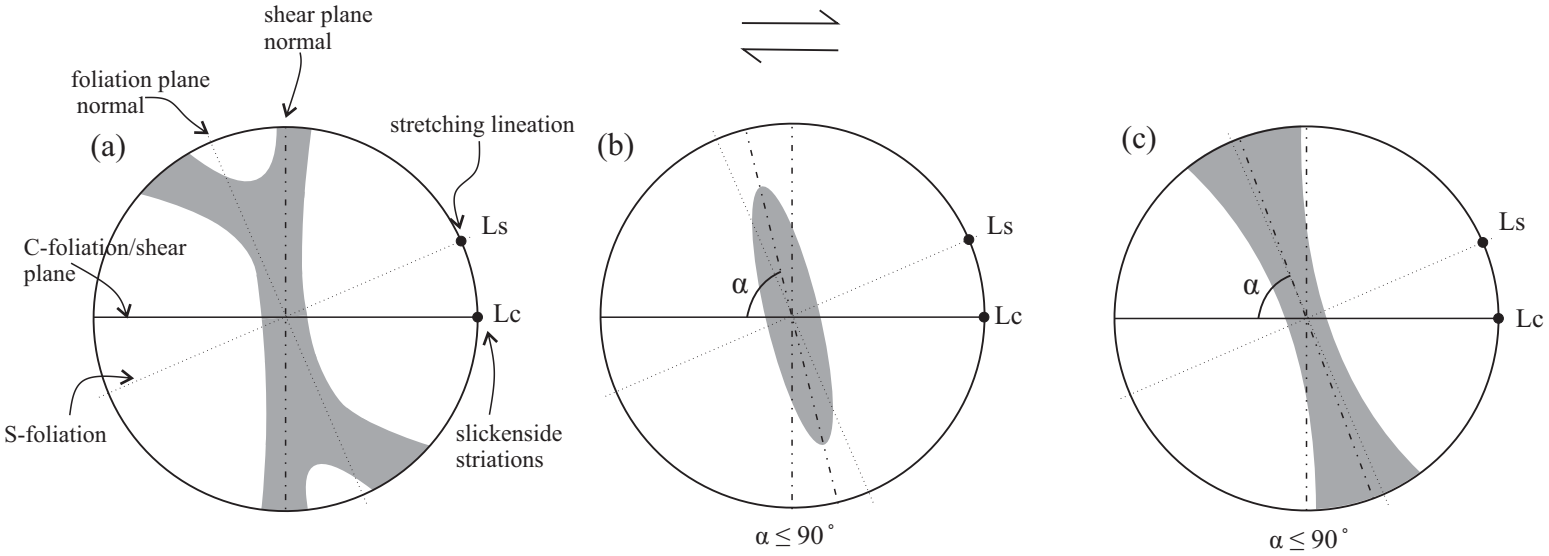
shear plane
normal
foliation plane
normal
(a)
stretching lineation
Ls
C-foliation/shear
plane
Lc
S-foliation
slickenside
striations
(b)
Ls
α
Lc
α ≤ 90 °
(c)
Ls
α
Lc
α ≤ 90 °

Figure 2.

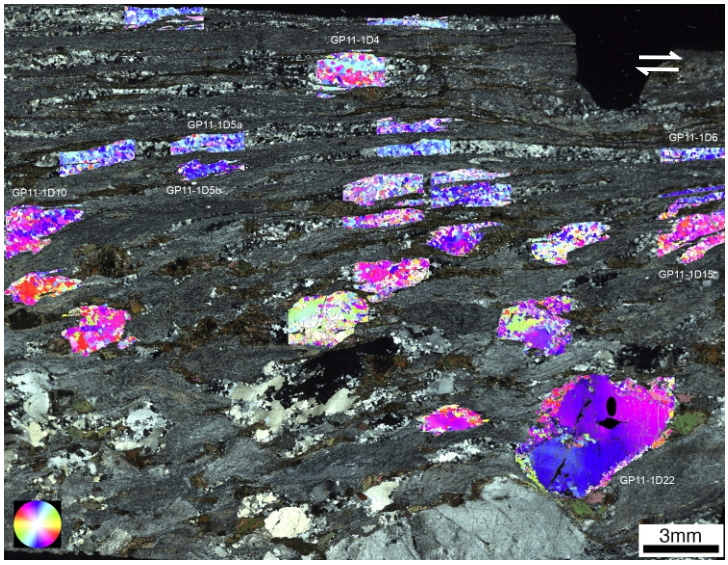

(a)

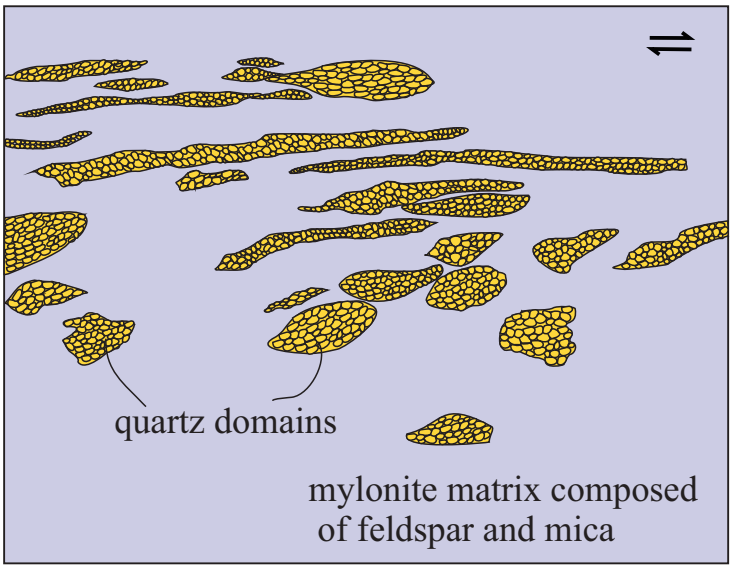

(b)

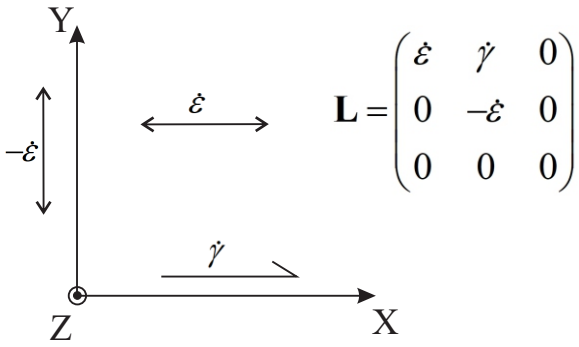

(c)

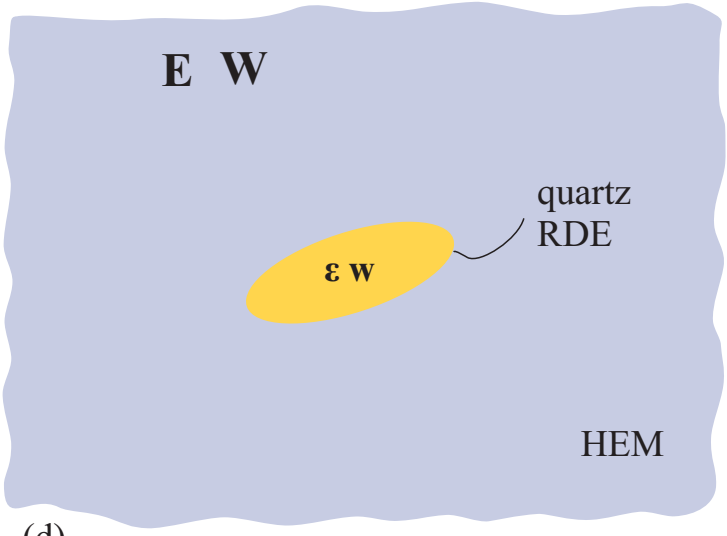

(d)

$$\boldsymbol{\varepsilon} = \mathbf{A}:\mathbf{E}$$

$$\mathbf{w} = \mathbf{W} + \boldsymbol{\Pi}:\mathbf{S}^{-1}:(\boldsymbol{\varepsilon} - \mathbf{E})$$

Figure 3.

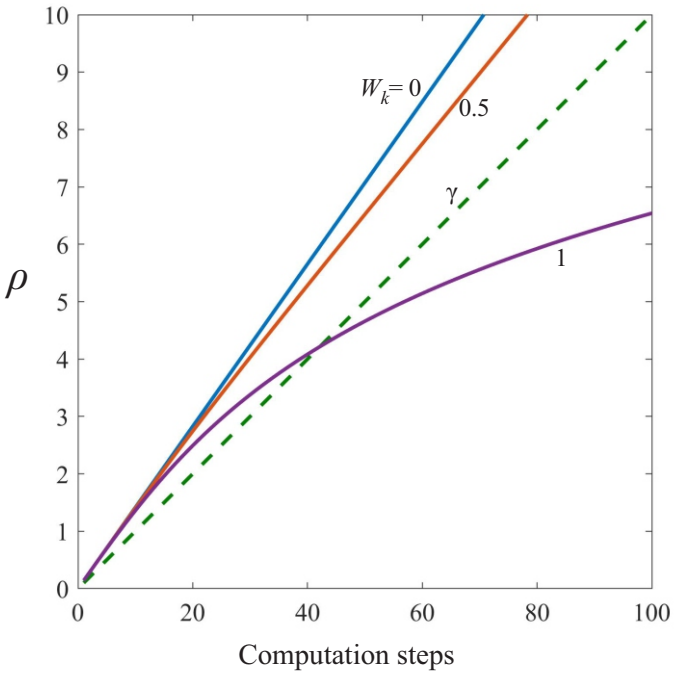
10
9
8
7
6
5
4
3
2
1
0
ρ
W_k= 0
0.5
γ
1
0
20
40
60
80
100
Computation steps

Figure 4.

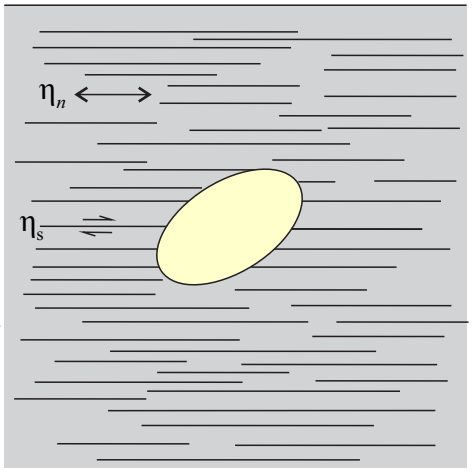

$$m = \frac{\eta_n}{\eta_s}$$

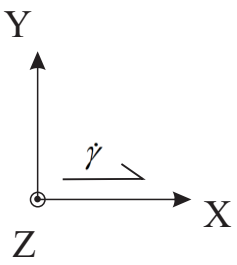

$$\mathbf{L} = \begin{pmatrix} 0 & \dot{\gamma} & 0 \\ 0 & 0 & 0 \\ 0 & 0 & 0 \end{pmatrix}$$

Figure 5.

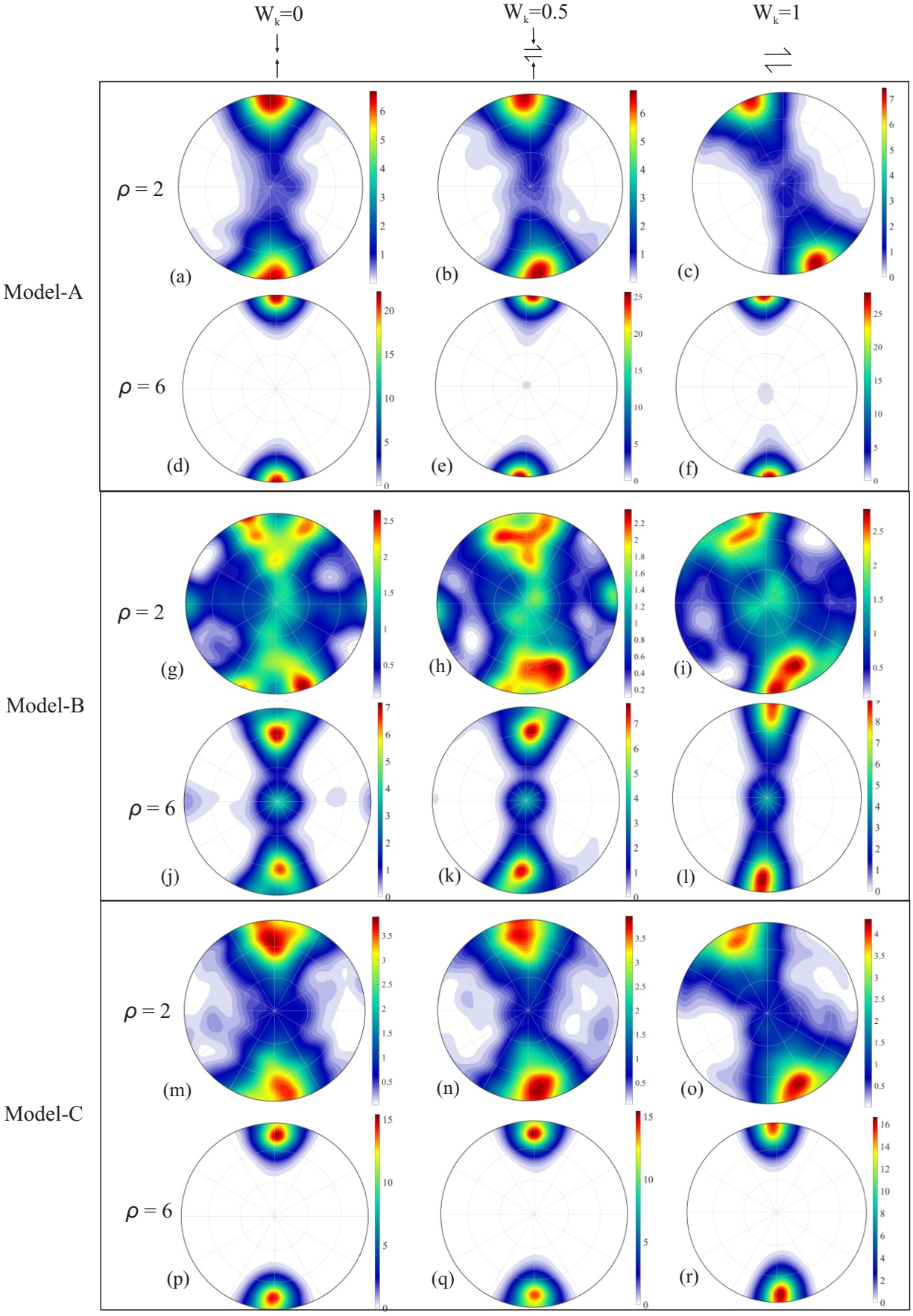
W_k=0
W_k=0.5
W_k=1
Model-A
Model-B
Model-C
ρ = 2
ρ = 6
(a)
(b)
(c)
(d)
(e)
(f)
(g)
(h)
(i)
(j)
(k)
(l)
(m)
(n)
(o)
(p)
(q)
(r)

Figure 6.

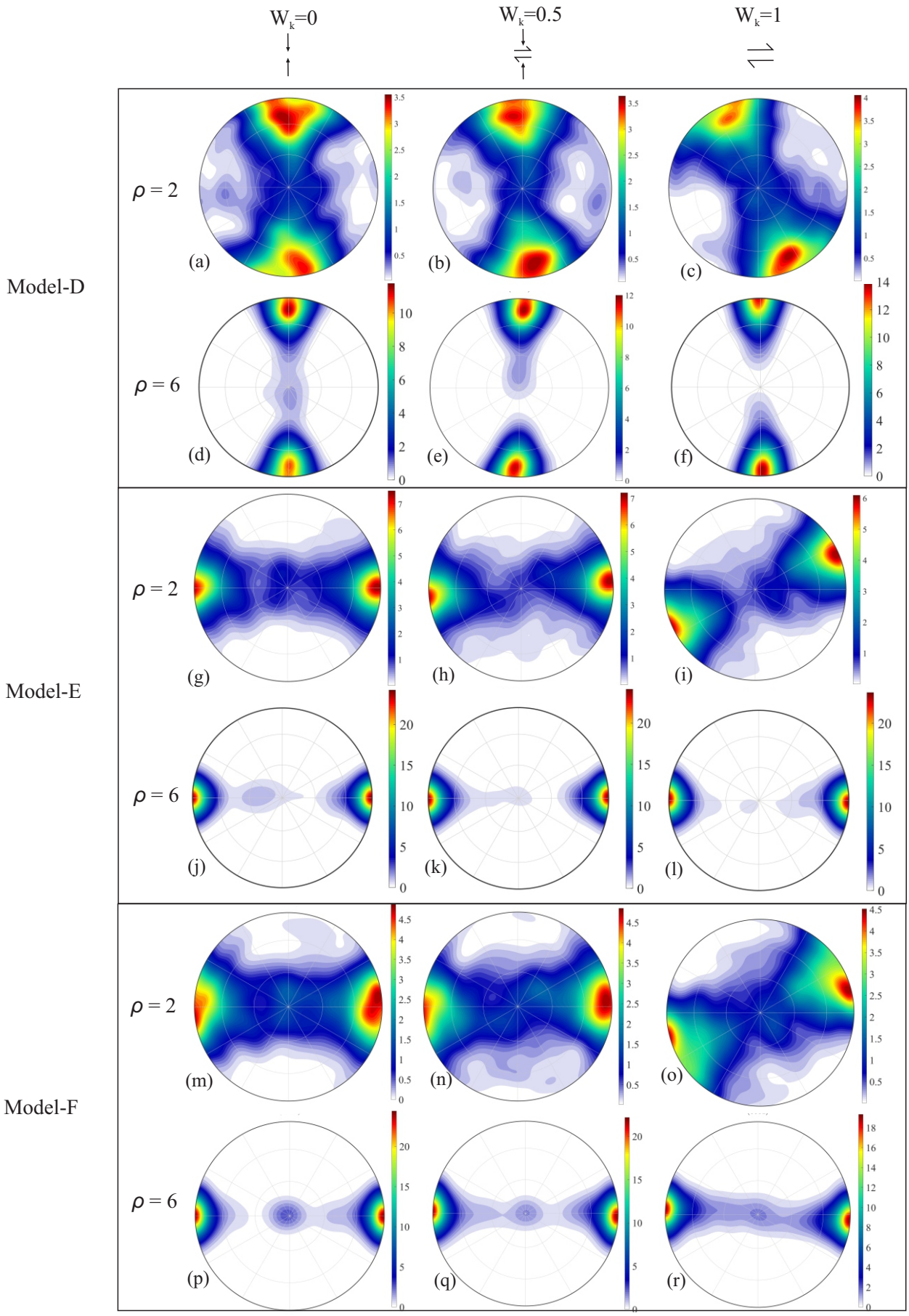
W_k=0
W_k=0.5
W_k=1
Model-D
Model-E
Model-F
ρ = 2
ρ = 6
(a)
(b)
(c)
(d)
(e)
(f)
(g)
(h)
(i)
(j)
(k)
(l)
(m)
(n)
(o)
(p)
(q)
(r)

Figure 7.

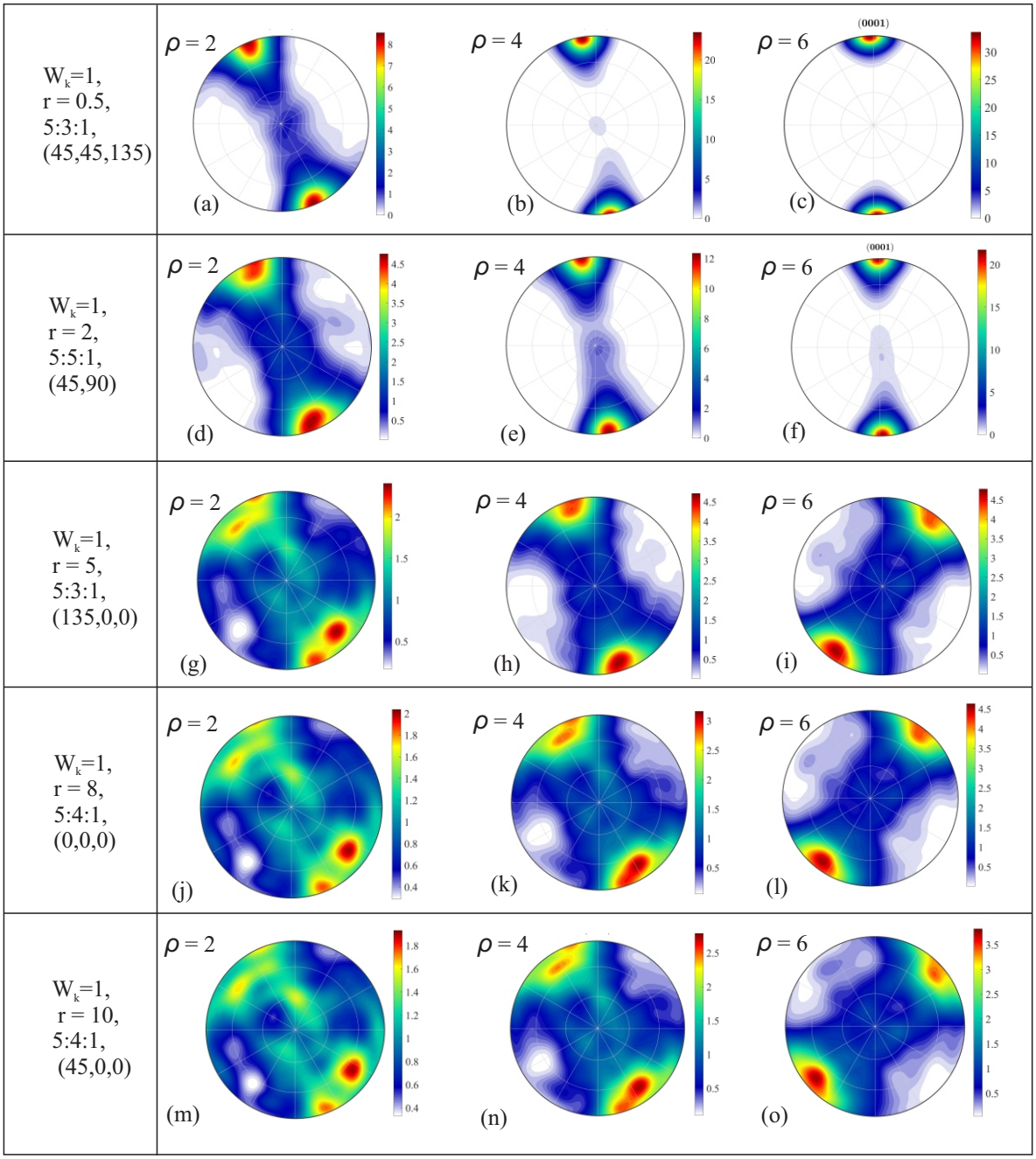
W_k=1, r = 0.5, 5:3:1, (45,45,135)
$\rho = 2$
(a)
$\rho = 4$
(b)
$\rho = 6$
(0001)
(c)
W_k=1, r = 2, 5:5:1, (45,90)
$\rho = 2$
(d)
$\rho = 4$
(e)
$\rho = 6$
(0001)
(f)
W_k=1, r = 5, 5:3:1, (135,0,0)
$\rho = 2$
(g)
$\rho = 4$
(h)
$\rho = 6$
(i)
W_k=1, r = 8, 5:4:1, (0,0,0)
$\rho = 2$
(j)
$\rho = 4$
(k)
$\rho = 6$
(l)
W_k=1, r = 10, 5:4:1, (45,0,0)
$\rho = 2$
(m)
$\rho = 4$
(n)
$\rho = 6$
(o)

Figure 8.

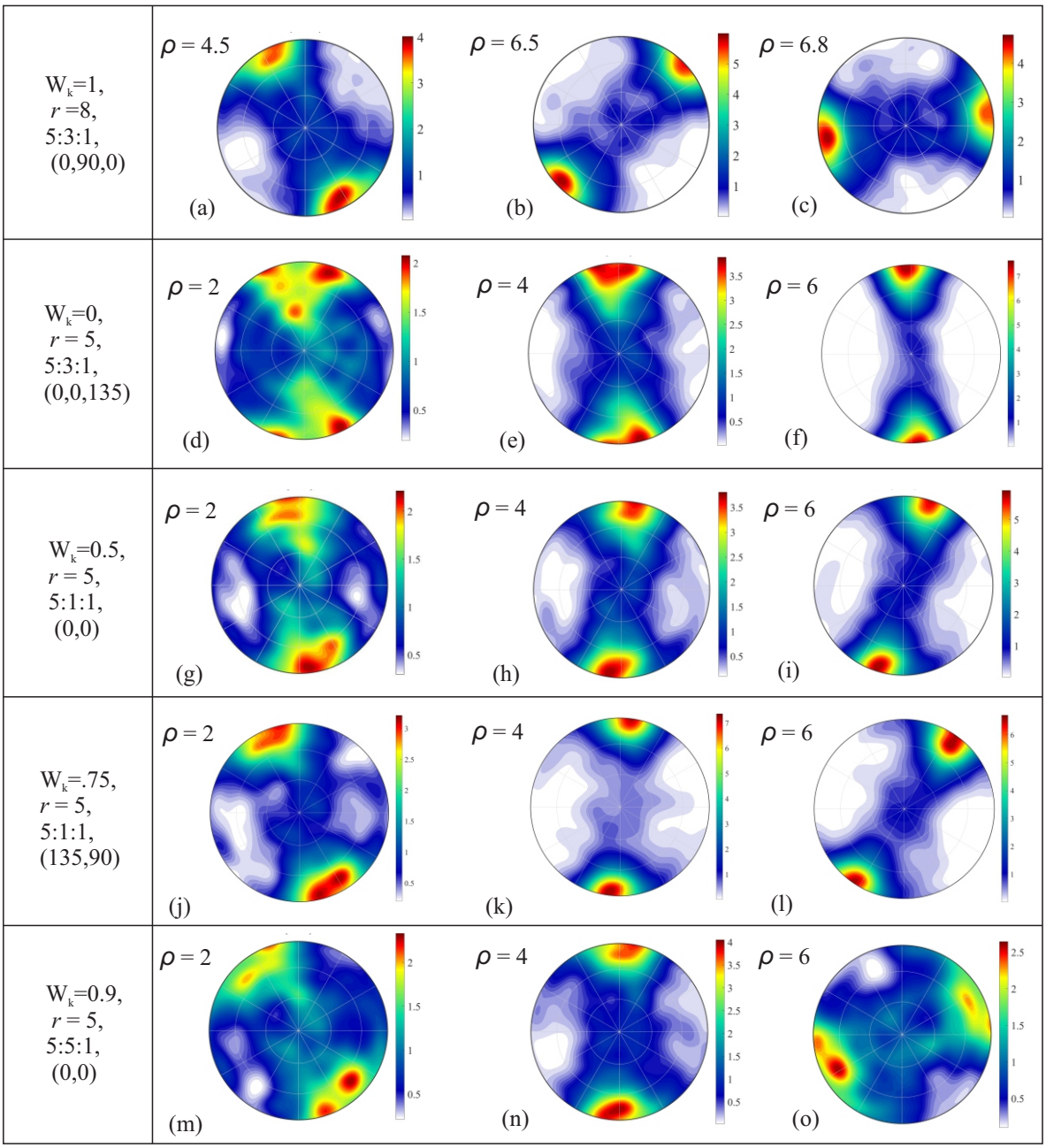
W_k=1, r=8, 5:3:1, (0,90,0)
ρ = 4.5
(a)
ρ = 6.5
(b)
ρ = 6.8
(c)
W_k=0, r = 5, 5:3:1, (0,0,135)
ρ = 2
(d)
ρ = 4
(e)
ρ = 6
(f)
W_k=0.5, r = 5, 5:1:1, (0,0)
ρ = 2
(g)
ρ = 4
(h)
ρ = 6
(i)
W_k=.75, r = 5, 5:1:1, (135,90)
ρ = 2
(j)
ρ = 4
(k)
ρ = 6
(l)
W_k=0.9, r = 5, 5:5:1, (0,0)
ρ = 2
(m)
ρ = 4
(n)
ρ = 6
(o)

Figure 9.

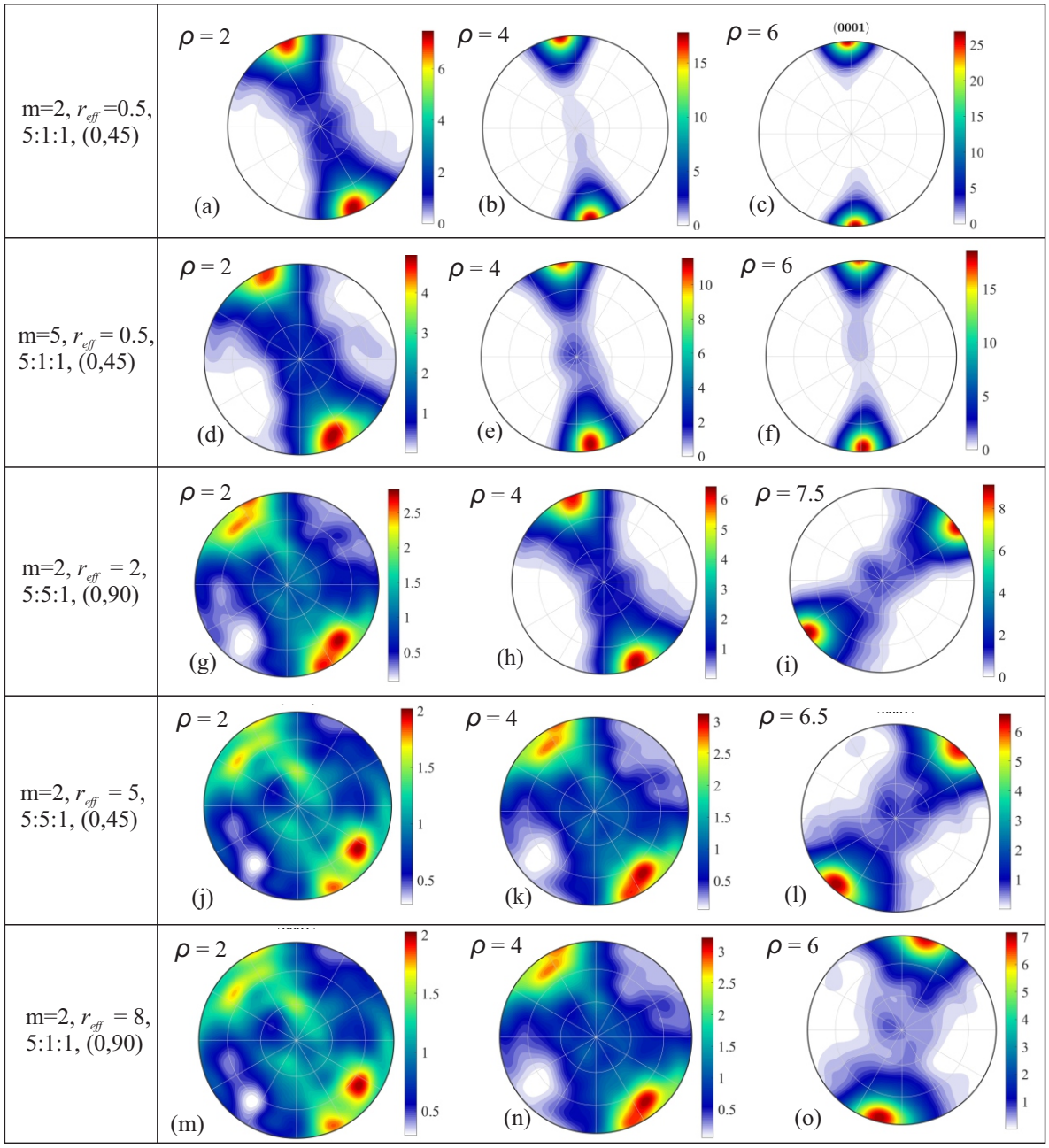
m=2, r_{eff}=0.5, 5:1:1, (0,45)
ρ = 2
(a)
ρ = 4
(b)
ρ = 6
(0001)
(c)
m=5, r_{eff} = 0.5, 5:1:1, (0,45)
ρ = 2
(d)
ρ = 4
(e)
ρ = 6
(f)
m=2, r_{eff} = 2, 5:5:1, (0,90)
ρ = 2
(g)
ρ = 4
(h)
ρ = 7.5
(i)
m=2, r_{eff} = 5, 5:5:1, (0,45)
ρ = 2
(j)
ρ = 4
(k)
ρ = 6.5
(l)
m=2, r_{eff} = 8, 5:1:1, (0,90)
ρ = 2
(m)
ρ = 4
(n)
ρ = 6
(o)

Figure 10.

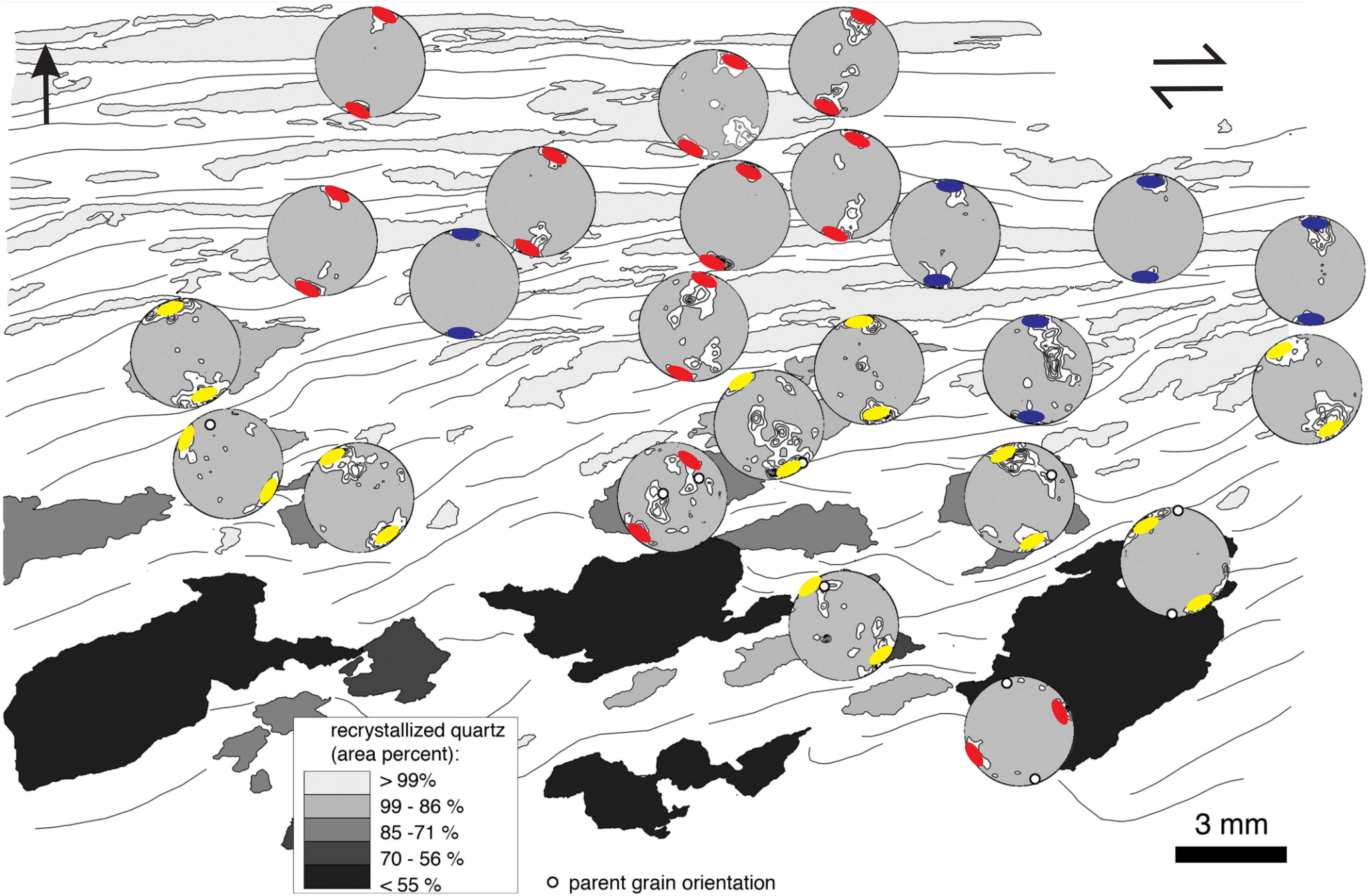
11
recrystallized quartz
(area percent):
> 99%
99 - 86 %
85 -71 %
70 - 56 %
< 55 %
parent grain orientation
3 mm

Figure 11.

W_k=1

W_k=0.75

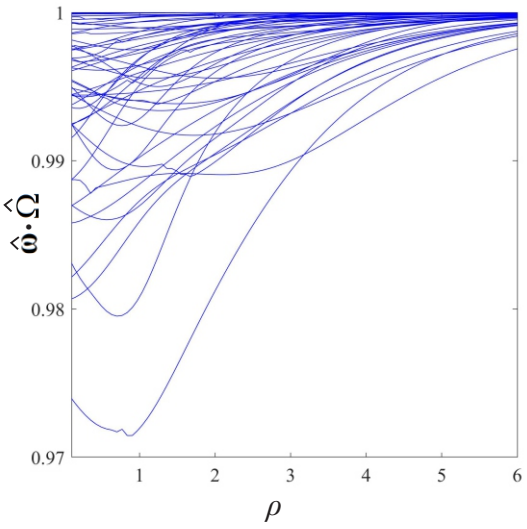

r =0.5

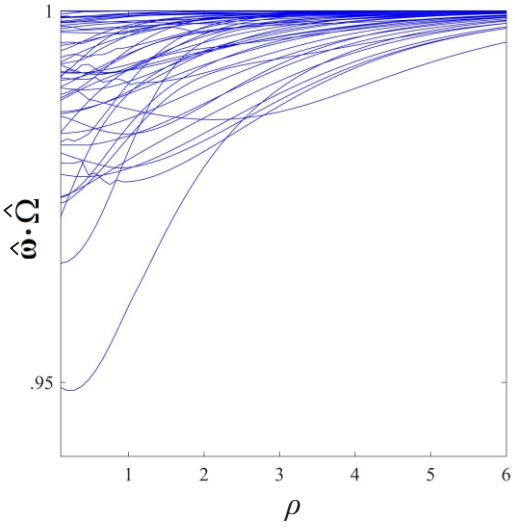

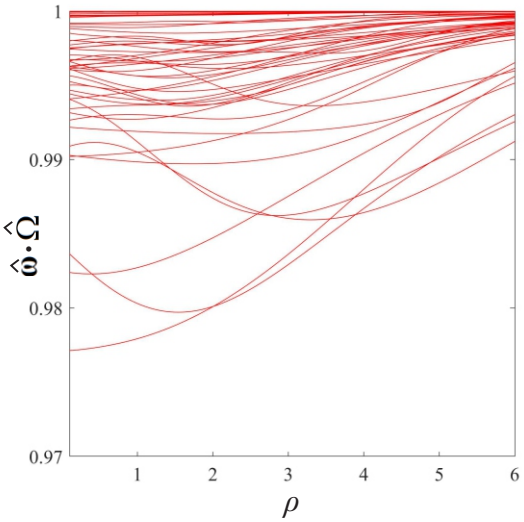

r = 2

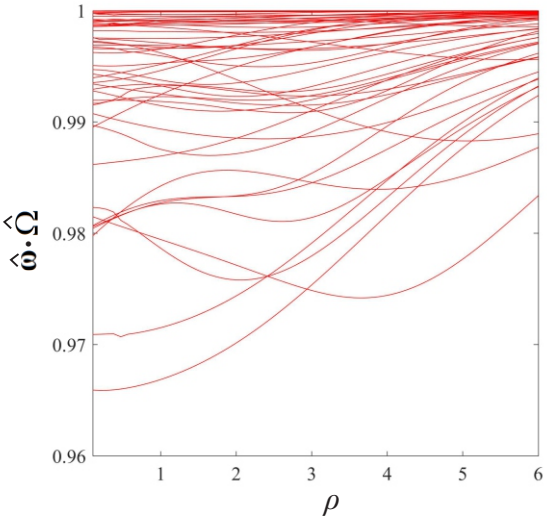

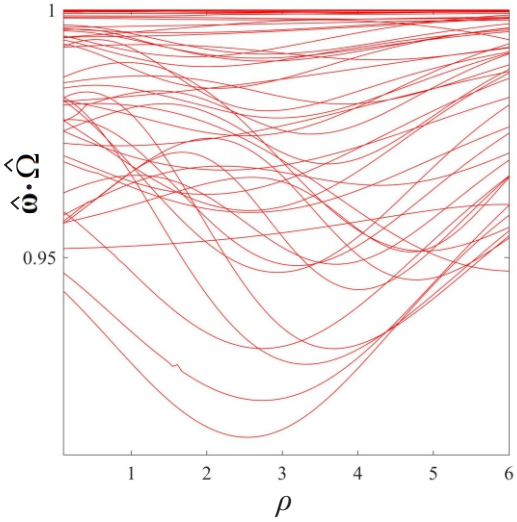

r = 5

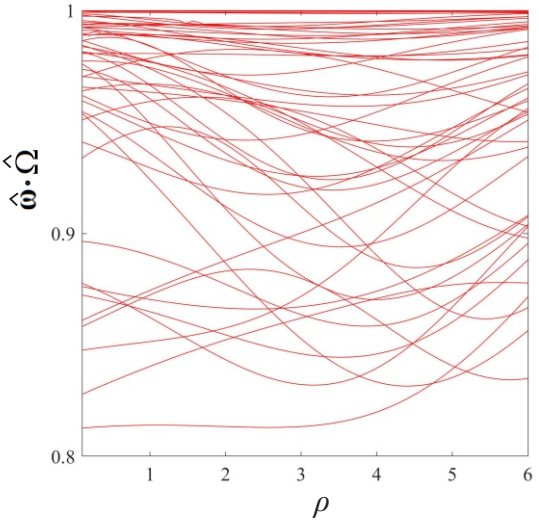

Slip Systems	CRSS ratio					
	Model A	Model B	Model C	Model D	Model E	Model F
Basal <a> $\{0001\}<\bar{1}2\bar{1}0>$	1	3	3	3	3	3
Rhomb<a> $\{10\bar{1}1\}<\bar{1}2\bar{1}0>$	5	5	1	1	5	3
Prismatic<a> $\{10\bar{1}0\}<\bar{1}2\bar{1}0>$	5	1	3	1	5	1
Prismatic <c> $\{10\bar{1}0\}<0001>$	10	10	10	10	1	1
Approximate Temperature Range	350-500˚C	500-600 ˚C	500-600 ˚C	500-600 ˚C	650 ˚C	650˚C